Article

Sol-gel synthesis and characterization of a quaternary bioglass for bone regeneration and tissue engineering

Ricardo Bento[1], Anuraag Gaddam[1], and José M.F. Ferreira[1] *

[1] Department of Materials and Ceramic Engineering, CICECO, University of Aveiro, 3810-193 Aveiro, Portugal; ricardobento@ua.pt; anuraagg@ua.pt

* Correspondent: jmf@ua.pt; Tel.: +351-234-370-242

Abstract:

In bone tissue engineering, ceramics have been the choice due to their excellent biological properties. But the paradigm changed with the discovery of bioactive glasses (BGs) in 1969 by Larry Hench and co-workers, due to their ability to bond to living tissues through the formation of an interfacial bone-like hydroxyapatite layer when the bioglass was put in contact with biological fluids *in vivo*. Among a number of tested compositions, the one exhibiting the highest bioactivity index is the well-known trademarked 45S5 Bioglass®. The topic received increasing attention particularly after 1985 when this material entered in the market of biomedical devices, inspiring many other investigations aiming at further exploring the *in vitro* and *in vivo* performances of this BG, or developing other related BG compositions. The research efforts gradually revealed a number of shortcomings of 45S5 Bioglass®, mostly derived from its high sodium content, initially intended to decrease the melting temperature and accelerating the degradation of the silicate network over time. But the extensive release of sodium from 45S5 Bioglass® in the biological fluids creates a high pH cytotoxic environment. Other serious drawbacks include a fast degradation rate, and a poor sintering ability, which hinders the reliable fabrication of porous scaffolds. Therefore, sol-gel was regarded as an attractive alternative to prepare alkali-free BG compositions. The process uses inorganic and/or organic precursors, which undergo hydrolysis and condensation at room-temperature, being less costly. When properly conducted, the sol-gel process might result in amorphous structures with all the components intimately mixed at the atomic scale. Moreover, developing new better performing materials for bone tissue engineering is a growing concern, as the ageing of the world's population leads to lower bone density and osteoporosis. This work describes the sol-gel synthesis of a novel quaternary silicate-based BG with the composition 60 SiO_2 – 34 CaO – 4 MgO – 2 P_2O_5 (mol%) was prepared using acidified distilled water as single solvent. By controlling the kinetics of the hydrolysis and condensation steps, an amorphous glass structure could be obtained. The results of XRD of samples calcined within the temperature range from 600-900 ºC demonstrated that amorphous nature was maintained until 800 ºC, followed by partial crystallization at 900 ºC. The specific surface area, an important factor in osteoconduction, was also evaluated over different temperatures, ranging from 160.6 ± 0.8 m^2/g at 600 ºC down to 2.2 ± 0.1 m^2/g at 900 ºC, being accompanied consistent changes in average pore size and agreeing pore size distribution. The immersion of the BG particles in simulated body fluid (SBF) led to the formation of an extensive apatite layer on its surface. These overall results indicate the proposed material is very promising for biomedical applications in bone regeneration and tissue engineering.

Keywords: Bioactive glasses; Alkali-free; Sol-gel; Bone regeneration; Tissue engineering.

1. Introduction

Life expectancy at birth is an important indicator of economic and social development. Noticeable increases in life expectancy were achieved along the two last centuries as well documented in several literature reports [1,2]. The overall scientific progresses achieved in the medical field, especially over the most recent decades, have also greatly contributed to an increase in the population's quality of life and, accordingly, to the increase of life expectancy. Of course, such great progresses bring together an unavoidable increase in the percentage of elderly population with social, economic and medical consequences [3,4]. As people grow older, they aren't as capable of physical exertion. This reduction of mechanical stimuli of the bones, along with the degradation of the tissues due to a lifetime of usage, increases the risk of fractures [5,6]. Due to this consequent increased incidence of bone-related diseases (osteoporosis, trauma fractures, removal of tumors, etc.), the researchers are faced with the task of providing new therapies and solutions that can prevent the onset of osteopathies and bone grafts are required to treat these ailments. Autografts, although being still considered the gold standard due to their optimal osteogenic, osteoinductive and osteoconductive properties, have multiple drawbacks, including the donor site morbidity and their limited availability [7]. On the other hand, allografts are often associated with risks of infection and a high non-union rate with host tissue [8,9]. Therefore, tissue engineering, and bone tissue engineering in particular, presents itself as a most promising alternative solution to the current bone grafting approaches [10].

Several materials have been tried and have achieved some success. Among these materials, bioceramics and bioglasses are promising candidates for bone regeneration owing to their natural properties such as biocompatibility, osteoinduction and osteoconduction adding to their composition which is similar to that of bone [11]. Dense ceramics, such as alumina [12,13] or zirconia [14–16], have found a wide use in load-bearing applications due to their excellent mechanical properties and low *in vivo* toxicity. In 1985, Hench et al. produced the first bioglass with commercial applications the 45S5 bioglass [17] and many more compositions were gradually disclosed since then [18–20]. Even though, these glasses possess excellent affinity with native bone, their commercial success has so far been relatively limited. Their drawbacks include inadequate mechanical properties and high dissolution rates of alkaline ions in biological conditions, which may have an harmful impact on cells [21–26], and several other shortcomings as well summarized elsewhere [27]. Oppositely, it was demonstrated that well designed alkali-free bioactive glass compositions offer a great number of advantages, including the ability to achieve full densification before the onset of crystallization, a fast bio-mineralization capability with the formation of a crystalline surface apatite layer after immersion in SBF solution for 1 h [28,29] and *in vivo* performances [30].

Traditionally, bioactive glasses are produced by melt-quenching. However, this technique implies higher energy costs and often results in bioglasses with crystalline phases, which have reduced biological properties and are unsuitable for producing porous scaffolds [11]. Due to this, sol-gel methods have been gaining notoriety as they yield glasses with higher purity and that are chemically and thermally stable as well as requiring low densification temperatures and allowing the production of a varied amount of compositions [31,32]. This technique does, however exhibit some drawbacks, namely the high cost of the precursors and the difficulty in producing dense, monolithic pieces [33].

2. Materials and Methods

2.1. Bioglass synthesis

A quaternary bioactive glass with composition consisting of 60 SiO_2 – 34 CaO – 4 MgO – 2 P_2O_5 (mol %) was prepared by sol-gel following a detailed procedure described elsewhere [32]. Tetraethyl

orthosilicate (TEOS, $Si(O_2H_5)$, ≥ 98 %) supplied by Sigma-Aldrich, and triethyl phosphate (TEP, $O_4P(C_2H_5O)$, ≥ 98 %) supplied by MERCK-Schuchardt, were used as Si and P network precursors, respectively; while calcium nitrate tetrahydrate ($Ca(NO_3)_2{\cdot}4\ H_2O$) supplied by Panreac, and magnesium nitrate hexahydrate ($Mg(NO_3)_2{\cdot}6\ H_2O$) supplied by Scharlau, were selected as Ca and Mg network modifiers, respectively. Nitric acid (HNO_3 ≥ 65 %) supplied by Labkem was used as catalysts to promote the hydrolysis of network precursors. Each preparation was planned to yield 0.2 mol of bioactive glass. Two separate aqueous solutions were initially prepared, one containing the network precursors, and the other the network modifiers. In brief, the required amounts of TEOS and TEP were added together to 20 mL of deionized water acidified with two drops of concentrated nitric acid, under magnetic stirring for 30 minutes until obtaining a transparent sol. The solution of the network modifiers was prepared in parallel by just adding the required amounts $Ca(NO_3)_2{\cdot}4\ H_2O$ and $Mg(NO_3)_2{\cdot}6\ H_2O$ to 20 mL of deionized water under magnetic stirring for 30 minutes. Due to their high solubility, this solution soon became transparent. Afterwards, both solutions were mixed together and magnetically stirred for further 60 minutes before being poured in Petri dishes and storing in an oven for 24 hours at 100 ºC to promote a relatively rapid sol-gel transition and drying. After 24 hours, the xerogel was crushed with an agate pestle & mortar into a fine powder and then heat treated at different temperatures.

2.2. Thermal treatment

Grounded xerogel powder was calcined for 2 hours at the following temperatures: 600, 700, 800 and 900 ºC with a heating rate of 0.5 ºC min^{-1}, and their properties were assessed through several characterization techniques, as described below.

2.3. XRD characterization

The powders' crystalline phase content was determined by x-ray diffraction (XRD, Rigaku Geigerflex D/Mac, C Series, Tokyo, Japan) using Cu K_α radiation with 2θ varying from 5-70º in steps of 0.026 s^{-1}.

2.4. FTIR characterization

The functional groups of the samples were analyzed by FTIR (FTIR Bruker Tensor 27) over the wavenumber range of 2000-300 cm^{-1}, with 256 scans and 4 cm^{-1} resolution.

2.5. SEM imaging

Specimens were covered with a thin (15 nm) carbon layer using a thin film deposition system (PVD 75, Kurt J. Lesker Co., Jefferson Hills, PA, USA) before being examined using a Hitachi S4100 Scanning Electron Microscope with a 15.0 kV accelerating voltage.

2.6. Specific surface area analysis

Specific surface area (SAA) and pore analyses was carried out with the BET, BJH and t-plot methods (Micrometric Gemini M-2380), N_2 was used as adsorbate and samples were previously degassed at 200 ºC.

2.7. SBF immersion assays

Powder samples were immersed in SBF for a period of 28 days. Every 7 days, the sample's reaction with the SBF was halted by filtering, rinsing with deionized, water and drying.

3. Results and Discussion

3.1. Bioglass synthesis - Effect of mixing time

XRD of the bioglasses prepared according to previous works [32] displayed an unexpected crystalline phase upon calcining at 600 ºC. Since we were in the winter season, an explanatory hypothesis for this was the prevailing lower room temperatures in the lab, which might have delayed the reaction kinetics. Therefore, the duration of the mixing step was increased from 30 to 60 minutes in order to allow complete hydrolysis. This longer mixing period successfully produced amorphous glasses as seen in **Figure 1**.

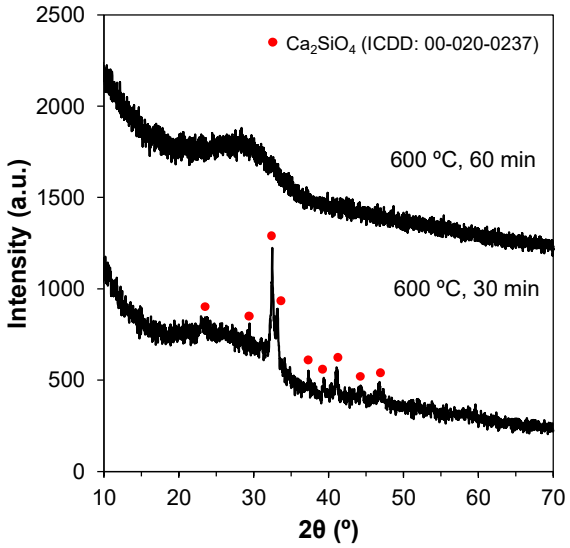

Figure 1. XRD patterns showing the effect of mixing times on producing amorphous glasses by the sol-gel method. Changing the mixing period from 30 to 60 minutes, produced amorphous glasses.

3.2. Effect of heat treatment temperature on the relevant properties of bioactive glass samples

Heat treating the sol-gel derived bioactive glasses is important to burn off the organics and release the nitrate ions from the Ca and Mg precursors. Increasing the heat treatment temperature enhances the densification of the material, affects its overall physical properties.

3.2.1. Crystalline phase assemblage

Heat treating beyond a certain temperature level is likely to promote devitrification. Therefore, the ideal heat treatment temperature for the sintering step can be assessed by XRD. **Figure 2** shows that the samples calcined within the temperature range 600-800 ºC remain amorphous. However, relatively well-defined crystalline peaks appear in the XRD pattern of the sample heat treated at 900 ºC. The crystalline phases were identified as silicon oxide (SiO_2), calcium silicate (Ca_2SiO_4), calcium phosphate ($Ca_3(PO_4)_2$ and calcium magnesium nitrate $Ca_3Mg(SiO_4)_2$. These results suggest that if an amorphous material is envisaged, the calcination temperature should not go much beyond 800 ºC.

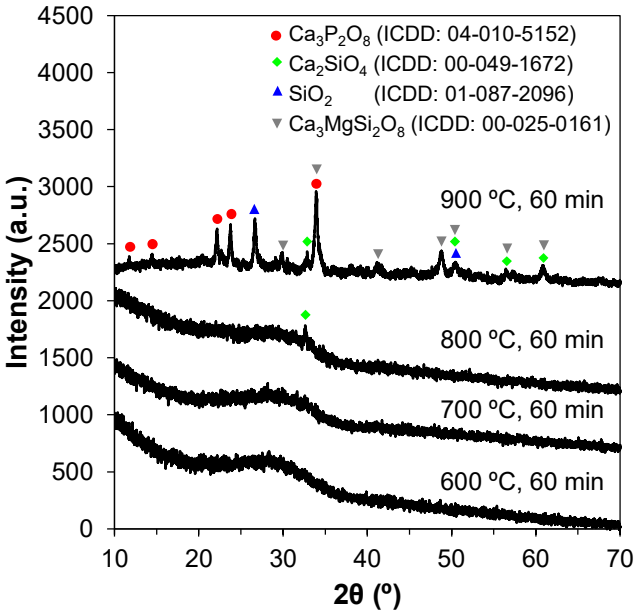

Figure 2. Effect of calcination temperature on glasses produced by the sol-gel method. Crystalline phases appear at 900 ºC.

3.2.2. Specific surface area

The impact of calcination temperature on the specific surface area (SSA) of the powders was assessed by resorting to gas adsorption of N_2, using the BET technique. The evolution of SSA as a function of temperature is present in **Figure 3**.

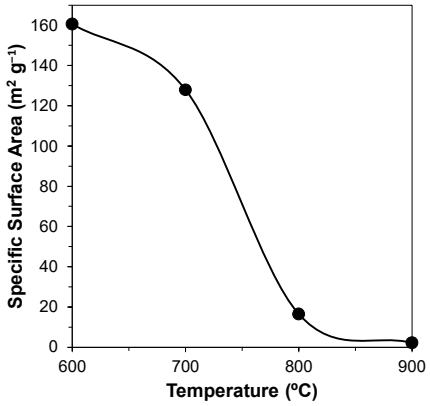

Figure 3. Effect of temperature on the specific surface area of the powders.

It can be seen that the SSA after calcination at 600 ºC is still relatively high (~160 $m^2 g^{-1}$), and gradually decreases to (~130 $m^2 g^{-1}$) with temperature increasing to 700 ºC. This is followed by a drastic change to (~16 $m^2 g^{-1}$) with further increasing the calcination temperature to 800 ºC, and then by a more gradually decrease to ~2–3 $m^2 g^{-1}$ upon heat treating at 900 ºC.

3.2.3. Adsorption and desorption isotherms

The porous structure profiles of the samples were initially investigated by analyzing their respective adsorption and desorption isotherms. These plots are present in **Figure 4**. After an initial intersection between adsorption and desorption curves at relatively low pressures, associated with

the formation of the N_2 monolayer, a hysteresis loop can be observed due to the condensation of the N_2 at higher pressures within the finer pores, creating multilayers. Such curves are classified as Type IV according to IUPAC. At 900 ºC, the curves do not intersect, producing an isothermal profile without a classification in IUPAC. It is known that the finer pores are the first to be eliminated due to their high driving force for densification. Accordingly, the average pore size tends to increase with increasing the heat treatment temperature. On the other hand, some pores might have shrunk into the microporous scale and become less accessible (more impervious) to gas exchanges. This explains why condensation is less evident for the sample calcined at 900 ºC, rendering the BET method ineffective at these ranges and producing an isotherm with an apparently open loop.

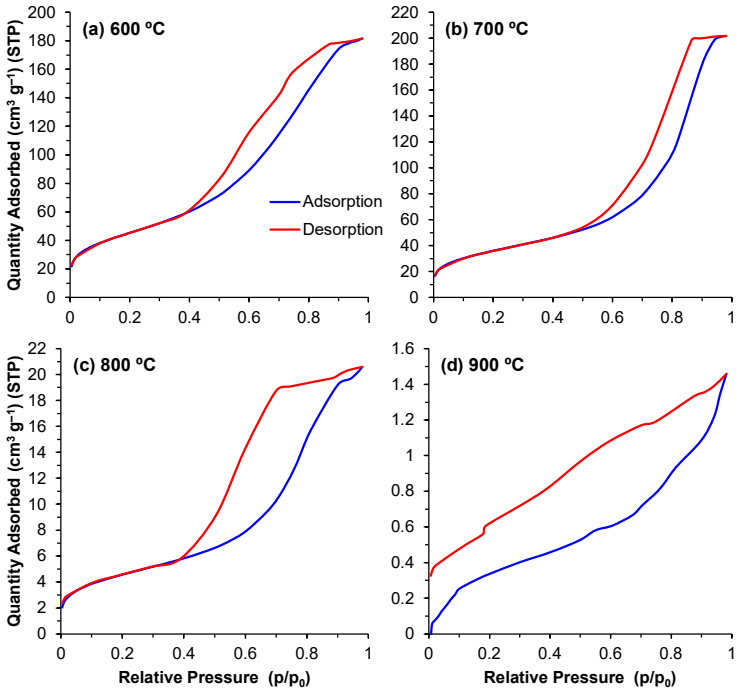

Figure 4. (a)—(d) Isotherm curves for powders calcined at temperatures 600— 900 ºC.

Regarding the different hysteresis loops found in these type IV isotherms, at 600 and 700 ºC, an H5 loop, characterized by a slight delay in desorption before a descending curve can be observed, pointing towards a structure where mesopores both open and partially blocked are present. For the powder sample calcined at 800 ºC, an H2(b) hysteresis can be observed indicated by the larger delay before a desorption with a steeper, quasi linear, descending curve. This loop also correlates to pore blocking but with a greater range of pore neck widths.

3.2.4. Pore size distribution

The pore distribution profiles obtained through the BJH method describe the surface area of these powders in even greater detail. The contributions of the different pore sizes to the overall surface area (dA/dlog(w)) and pore volume (dV/dlog(w)) are displayed in **Figures 5 and 6**, respectively. For all powders, the majority of the contribution to the total area and pore volume came from pores within the 18-200 Å range. The data depict the aforementioned decrease in total surface area and volume, however, the same data also depict and interesting trend regarding the porous evolution of these samples. Comparing the samples calcined at 600 ºC with those calcined at 700 ºC, the decrease in surface area is paired with a shift of the relative contribution to the total area from the smaller pores to larger ones. From 700 ºC up to 900 ºC, this trend is reversed and we observe the major contribution

to the total values comes from increasingly smaller pore ranges, highlighting the transition from a mesoporous to a microporous material. This shift is likely derived from the closure of the smaller pores in the 600-700 ºC transition which means the larger pores, which are still open, being the main responsible factor for the measured surface area. With further increases in temperature, these pores will continue shrinking resulting in smaller pores at the 800 and 900 ºC samples.

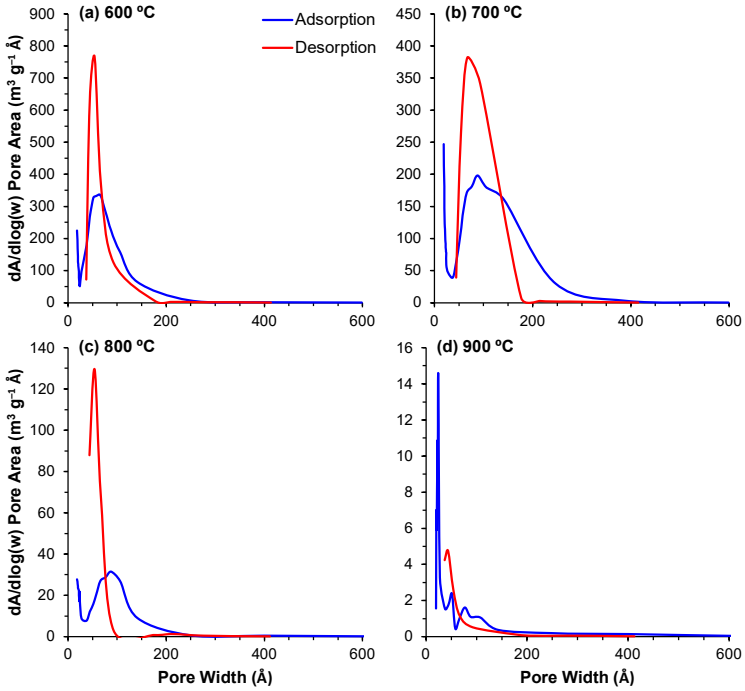

Figure 5. (a)—(d) Contribution of the different pore sizes to the overall surface area for the powders calcined at the different temperatures 600— 900 ºC.

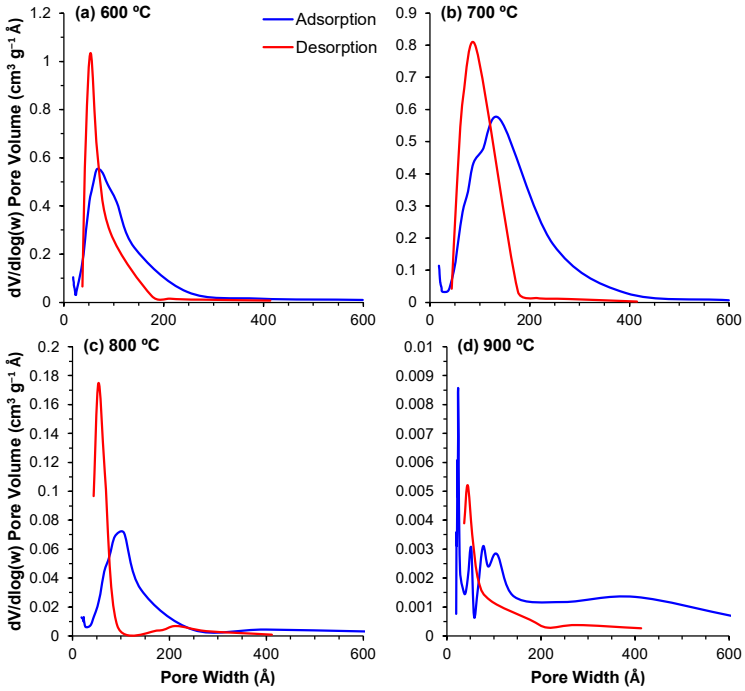

Figure 6. (a)—(d) Contribution of the different pore sizes to the overall pore volume for the powders calcined at the different temperatures 600— 900 ºC.

3.3. Bioactivity assessment through SBF immersion assays

Bioactivity of the bioglass powders was assessed by immersion in simulated body fluid (SBF) over a period of 28 days. Considering the generally high SSA values of the samples, the amount of powder that was added per mL of the SBF solution was double relatively to the standard ratio of 0.5 cm^2 mL^{-1} proposed by Popa et al. [34] for bulk samples, calculated according to the following equation:

$$SM = \frac{\rho \cdot SA \cdot D}{6}$$

where SM is the sample mass in grams, ρ is the density in grams per cubic centimeter, SA is the sample area in square centimeters exposed to the SBF solution and D is the average particle diameter in centimeters. The tested powders were assumed to be perfect spheres with a diameter of ~1.25 x 10^{-2} **cm** (~125 μm, the average aperture size of the two sieves used, 150 μm and 100 μm). For 20 mL of SBF, 0.0572 g of bioglass powder was added. Samples were retrieved every 7 days, and the reaction halted, and were afterwards analyzed resorting to XRD and FTIR measurements as well as through scanning electron microscopy.

3.3.1. XRD patterns

The XRD patterns for the SBF treated glass powders can be seen in **Figure 7**. A calcium phosphate and calcite were the two phases formed onto the surface of the particles. Peaks at 24 and 32º are present for all tested time points and can be associated with apatite reflections. Other peaks in the regions around 29, 40, 47 and 50º are attributed to apatite reflections as well. These crystalline peaks indicate the presence of a hydroxyapatite layer on the powders' surface. Both crystalline phases formed are bioactive and prone to the binding between the implant material and the living tissues.

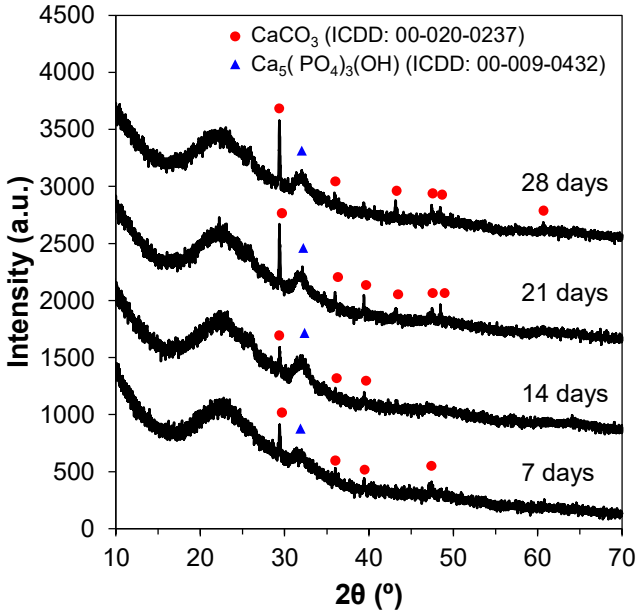

Figure 7. XRD patterns of powders (calcined at 600 ºC) immersed in SBF from 7 to28 days.

3.3.2. FTIR spectra

FTIR spectra further point towards the formation of a hydroxyapatite layer, as seen in **Figure 8a**. The spectra reveals the three main vibrational modes of the Si–O–Si groups, namely: the peaks in the 1000 – 1100 cm^{-1} range are associated with the stretching vibration of the Si–O–Si groups with the bridging oxygens moving opposite of the silicone; at ~780 cm^{-1} a peak associated with the bending vibration of the Si–O–Si group, characterized by the oxygen atom moving at right angles; and finally at 500 cm^{-1} the rocking vibration of the Si–O–Si is observed. Phosphate groups can also be identified by the peak at 600 cm^{-1} assigned to asymmetric bending. The peak at the ~1500–1550 cm^{-1} range is associated with a C-O stretch indicating that carbon from the atmosphere may have reacted with calcium from the powders to form carbonates. Another carbonate stretching vibration can be observed at ~1300 cm^{-1} related to unhydrolyzed residual organics from the sol-gel step. Finally, the band located at ~1600 cm^{-1} is attributed to the hydrogen bonded to water which was absorbed in the sample [35–37]. To better understand the formation of hydroxyapatite due to SBF, the spectra were subtracted with the base glass, corresponding to 0 days, as seen in **Figure 8b**. The subtracted spectra reveal peaks at 1384, 1147, 968, 854, 744, 669, and 518 cm^{-1}, **wh**ich correspond to the following vibrational modes: asymmetric stretching of $(CO_3)^{2-}$, asymmetric stretching of $(PO_4)^{3-}$, symmetric stretching of $(PO_4)^{3-}$, asymmetric bending of $(CO_3)^{2-}$, symmetric bending of $(CO_3)^{2-}$, stretching of $(PO_4)^{3-}$, and bending of $(PO_4)^{3-}$, respectively [37]. The spectra show that with increasing number of days, the amount hydroxyapatite also increases.

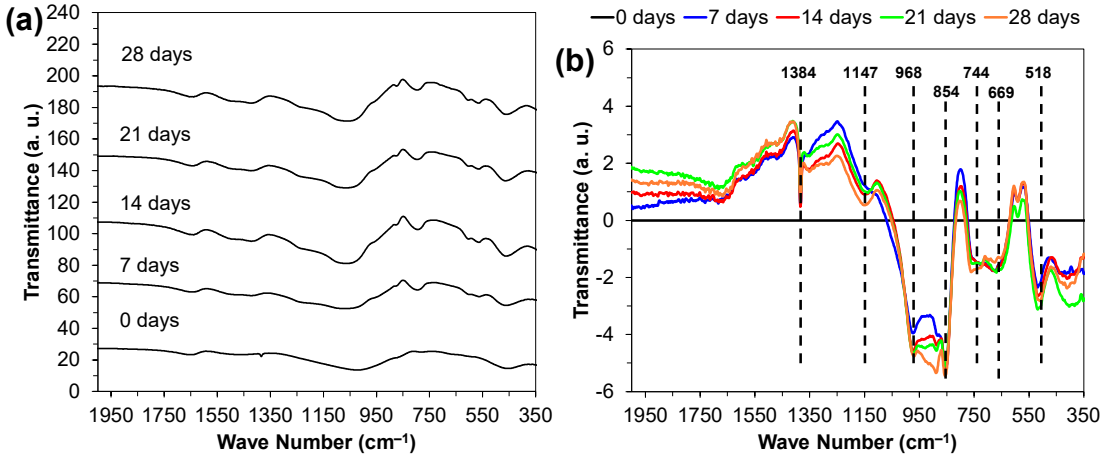

Figure 8. (a) FTIR spectra for powders that were calcined at 600 ºC before immersing in SBF for different durations; (b) FTIR spectra with 0 days' sample base line subtracted.

3.3.3. SEM images

SEM observations further sustain the previous data by showing a relatively smooth surface for the control powder samples (0 days, calcined at 600 ºC) whereas after 28 days a rugged apatite surface with small circular apatite crystals can be observed, **Figure 9**.

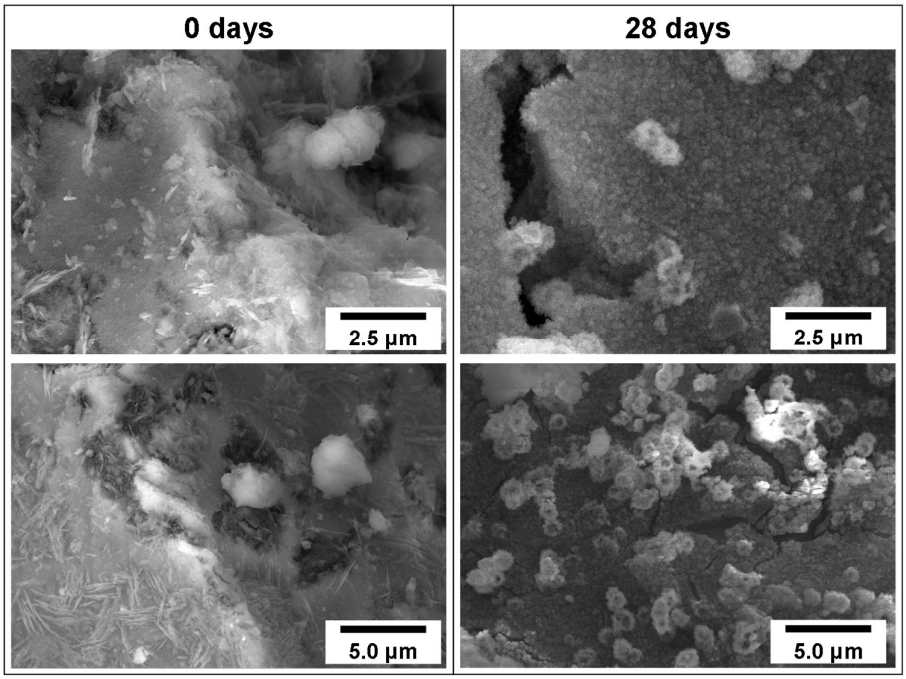

Figure 9. SEM images of powder (calcined at 600 ºC) surfaces before (0 days) and after immersion in SBF for 28 days, confirming the formation of an appetite layer.

4. Conclusion

This work reports on the fabrication and processing of a new bioglass belonging to the SiO_2-CaO-MgO-P_2O_5 system by sol-gel method. The effect of calcination temperature on the crystalline phase assemblage and on the specific surface area of these powders was studied. The results show an accentuated decreasing trend in the surface area with increasing temperature. At temperatures >> 800 ºC, the samples undergo crystallization. According to BET results, the sample calcined at 600 ºC shows the highest surface area, thus being suitable for biological applications, including the storage and release of pharmaceutical drugs. This sample also shows the formation of hydroxyapatite layer after only 7 days of SBF treatment, being therefore a promising material for future applications in bone regeneration and tissue engineering.

Acknowledgments

This work was developed within the scope of the project CICECO-Aveiro Institute of Materials, FCT Ref. UID/CTM/50011/2019, financed by national funds through the Portuguese Foundation for Science and Technology (FCT/MCTES).

References

1. Biggs, B.; King, L.; Basu, S.; Stuckler, D. Is wealthier always healthier? The impact of national income level, inequality, and poverty on public health in Latin America. *Soc. Sci. Med.* **2010**, *71*, 266–273, doi:10.1016/j.socscimed.2010.04.002.

2. Clark, R. World health inequality: Convergence, divergence, and development. *Soc. Sci. Med.* **2011**, *72*, 617–624, doi:10.1016/j.socscimed.2010.12.008.

3. Galasso, V.; Profeta, P. The political economy of social security: a survey. *Eur. J. Polit. Econ.* **2002**, *18*, 1–29, doi:https://doi.org/10.1016/S0176-2680(01)00066-0.

4. Orlická, E. Impact of Population Ageing and Elderly Poverty on Macroeconomic Aggregates. *Procedia Econ. Financ.* **2015**, *30*, 598–605, doi:https://doi.org/10.1016/S2212-5671(15)01272-1.

5. Wilson, R.T.; Chase, G.A.; Chrischilles, E.A.; Wallace, R.B. Hip Fracture Risk Among Community-Dwelling Elderly People in the United States: A Prospective Study of Physical, Cognitive, and Socioeconomic Indicators. *Am. J. Public Health* **2006**, *96*, 1210–1218, doi:10.2105/AJPH.2005.077479.

6. Ngugyen, T. V; Eisman, J.A.; Kelly, P.J.; Sambroak, P.N. Risk Factors for Osteoporotic Fractures in Elderly Men. *Am. J. Epidemiol.* **1996**, *144*, 255–263, doi:10.1093/oxfordjournals.aje.a008920.

7. Sen, M.K.; Miclau, T. Autologous iliac crest bone graft: Should it still be the gold standard for treating nonunions? *Injury* **2007**, *38*, S75–S80, doi:10.1016/j.injury.2007.02.012.

8. Nandi, S.K.; Roy, S.; Mukherjee, P.; Kundu, B.; De, D.K.; Basu, D. Orthopaedic applications of bone graft & graft substitutes: a review. *Indian J. Med. Res.* **2010**, *132*, 15–30.

9. Greenwald, M.A.; Kuehnert, M.J.; Fishman, J.A. Infectious disease transmission during organ and tissue transplantation. *Emerg. Infect. Dis.* **2012**, *18*, e1, doi:10.3201/eid1808.120277.

10. Roseti, L.; Parisi, V.; Petretta, M.; Cavallo, C.; Desando, G.; Bartolotti, I.; Grigolo, B. Scaffolds for Bone Tissue Engineering: State of the art and new perspectives. *Mater. Sci. Eng. C* **2017**, *78*, 1246–1262, doi:10.1016/j.msec.2017.05.017.

11. Jones, J.R. Review of bioactive glass : From Hench to hybrids. *Acta Biomater.* **2013**, *9*, 4457–4486, doi:10.1016/j.actbio.2012.08.023.

12. Mohanty, M. Medical Applications of Alumina Ceramics. *Trans. Indian Ceram. Soc.* **1995**, *54*, 200–204, doi:10.1080/0371750X.1995.10804720.

13. Rahmati, M.; Mozafari, M. Biocompatibility of alumina-based biomaterials–A review. *J. Cell. Physiol.* **2019**, *234*, 3321–3335, doi:https://doi.org/10.1002/jcp.27292.

14. Li, K.; Chen, J.; Peng, J.; Koppala, S.; Omran, M.; Chen, G. One-step preparation of CaO-doped partially stabilized zirconia from fused zirconia. *Ceram. Int.* **2020**, *46*, 6484–6490, doi:https://doi.org/10.1016/j.ceramint.2019.11.129.

15. Manicone, P.F.; Rossi Iommetti, P.; Raffaelli, L. An overview of zirconia ceramics: basic properties and clinical applications. *J. Dent.* **2007**, *35*, 819–826, doi:10.1016/j.jdent.2007.07.008.

16. Chen, Y.-W.; Moussi, J.; Drury, J.L.; Wataha, J.C. Zirconia in biomedical applications. *Expert Rev. Med. Devices* **2016**, *13*, 945–963, doi:10.1080/17434440.2016.1230017.

17. Hench, L.L. Bioceramics: From Concept to Clinic. *J. Am. Ceram. Soc.* **1991**, *74*, 1487–1510, doi:10.1111/j.1151-2916.1991.tb07132.x.

18. Montazerian, M.; Dutra Zanotto, E. History and trends of bioactive glass-ceramics. *J. Biomed. Mater. Res. Part A* **2016**, *104*, 1231–1249, doi:https://doi.org/10.1002/jbm.a.35639.

19. Kaur, G.; Pandey, O.P.; Singh, K.; Homa, D.; Scott, B.; Pickrell, G. A review of bioactive glasses: Their structure, properties, fabrication and apatite formation. *J. Biomed. Mater. Res. Part A* **2014**, *102*, 254–274, doi:https://doi.org/10.1002/jbm.a.34690.

20. Hum, J.; Boccaccini, A.R. Bioactive glasses as carriers for bioactive molecules and therapeutic drugs: a review. *J. Mater. Sci. Mater. Med.* **2012**, *23*, 2317–2333, doi:10.1007/s10856-012-4580-z.

21. Ciraldo, F.E.; Boccardi, E.; Melli, V.; Westhauser, F.; Boccaccini, A.R. Tackling bioactive glass excessive in vitro bioreactivity: Preconditioning approaches for cell culture tests. *Acta Biomater.* **2018**, *75*, 3–10, doi:https://doi.org/10.1016/j.actbio.2018.05.019.

22. Gubler, M.; Brunner, T.J.; Zehnder, M.; Waltimo, T.; Sener, B.; Stark, W.J. Do bioactive glasses convey a disinfecting mechanism beyond a mere increase in pH? *Int. Endod. J.* **2008**, *41*, 670–678, doi:https://doi.org/10.1111/j.1365-2591.2008.01413.x.

23. Peitl, O.; Dutra Zanotto, E.; Hench, L.L. Highly bioactive P2O5–Na2O–CaO–SiO2 glass-ceramics. *J. Non. Cryst. Solids* **2001**, *292*, 115–126, doi:10.1016/S0022-3093(01)00822-5.

24. Heimke, G.; Griss, P. Ceramic implant materials. *Med. Biol. Eng. Comput.* **1980**, *18*, 503–510, doi:10.1007/BF02443328.

25. Crovace, M.C.; Souza, M.T.; Chinaglia, C.R.; Peitl, O.; Zanotto, E.D. Biosilicate® — A multipurpose, highly bioactive glass-ceramic. In vitro, in vivo and clinical trials. *J. Non. Cryst. Solids* **2016**, *432*, 90–110, doi:10.1016/j.jnoncrysol.2015.03.022.

26. Westhauser, F.; Hohenbild, F.; Arango-Ospina, M.; Schmitz, S.I.; Wilkesmann, S.; Hupa, L.; Moghaddam, A.; Boccaccini, A.R. Bioactive Glass (BG) ICIE16 Shows Promising Osteogenic Properties Compared to Crystallized 45S5-BG. *Int. J. Mol. Sci.* **2020**, *21*, 1639, doi:10.3390/ijms21051639.

27. Fernandes, H.R.; Gaddam, A.; Rebelo, A.; Brazete, D.; Stan, G.E.; Ferreira, J.M.F. Bioactive Glasses and Glass-Ceramics for Healthcare Applications in Bone Regeneration and Tissue Engineering. *Materials (Basel).* **2018**, *11*, 2530, doi:10.3390/ma11122530.

28. Goel, A.; Kapoor, S.; Rajagopal, R.R.; Pascual, M.J.; Kim, H.-W.; Ferreira, J.M.F. Alkali-free bioactive glasses for bone tissue engineering: A preliminary investigation. *Acta Biomater.* **2012**, *8*, 361–372, doi:10.1016/j.actbio.2011.08.026.

29. Kapoor, S.; Semitela, Â.; Goel, A.; Xiang, Y.; Du, J.; Lourenço, A.H.; Sousa, D.M.; Granja, P.L.; Ferreira, J.M.F. Understanding the composition-structure-bioactivity relationships in diopside ($CaO{\cdot}MgO{\cdot}2SiO_2$)-tricalcium phosphate ($3CaO{\cdot}P_2O_5$) glass system. *Acta Biomater.* **2015**, *15*, 210–226, doi:10.1016/j.actbio.2015.01.001.

30. Cortez, P.P.; Brito, A.F.; Kapoor, S.; Correia, A.F.; Atayde, L.M.; Dias-Pereira, P.; Maurício,

A.C.; Afonso, A.; Goel, A.; Ferreira, J.M.F. The *in Vivo* Performance of an Alkali-free Bioactive Glass for Bone Grafting, FastOs®BG, Assessed with an Ovine. *J. Biomed. Mater. Res. Part B Appl. Biomater.* **2017**, *105*, 30–38, doi:10.1002/jbm.b.33529.

31. Bellucci, D.; Sola, A.; Salvatori, R.; Anesi, A.; Chiarini, L.; Cannillo, V. Sol-gel derived bioactive glasses with low tendency to crystallize: synthesis, post-sintering bioactivity and possible application for the production of porous scaffolds. *Mater. Sci. Eng. C. Mater. Biol. Appl.* **2014**, *43*, 573–586, doi:10.1016/j.msec.2014.07.037.

32. Ben-Arfa, B.A.E.; Miranda Salvado, I.M.; Ferreira, J.M.F.; Pullar, R.C. A hundred times faster: Novel, rapid sol-gel synthesis of bio-glass nanopowders (Si-Na-Ca-P system, Ca:P = 1.67) without aging. *Int. J. Appl. Glas. Sci.* **2017**, *8*, 337–343, doi:https://doi.org/10.1111/ijag.12255.

33. Schmidt, H. Chemistry of material preparation by the sol-gel process. *J. Non. Cryst. Solids* **1988**, *100*, 51–64, doi:https://doi.org/10.1016/0022-3093(88)90006-3.

34. Popa, A.C.; Stan, G.E.; Husanu, M.A.; Mercioniu, I.; Santos, L.F.; Fernandes, H.R.; Ferreira, J.M.F. Bioglass implant-coating interactions in synthetic physiological fluids with varying degrees of biomimicry. *Int. J. Nanomedicine* **2017**, *12*, 683–707, doi:10.2147/IJN.S123236.

35. Dziadek, M.; Zagrajczuk, B.; Jelen, P.; Olejniczak, Z.; Cholewa-Kowalska, K. Structural variations of bioactive glasses obtained by different synthesis routes. *Ceram. Int.* **2016**, *42*, 14700–14709, doi:10.1016/j.ceramint.2016.06.095.

36. Agathopoulos, S.; Tulyaganov, D.U.; Ventura, J.M.G.; Kannan, S.; Karakassides, M.A.; Ferreira, J.M.F. Formation of hydroxyapatite onto glasses of the CaO-MgO-SiO_2 system with B_2O_3, Na_2O, CaF_2 and P_2O_5 additives. *Biomaterials* **2006**, *27*, 1832–1840, doi:10.1016/j.biomaterials.2005.10.033.

37. Aguiar, H.; Serra, J.; González, P.; León, B. Structural study of sol–gel silicate glasses by IR and Raman spectroscopies. *J. Non. Cryst. Solids* **2009**, *355*, 475–480, doi:10.1016/j.jnoncrysol.2009.01.010.